OPEN ACCESS

Electrochemical Stability Window and Electrolyte Breakdown Mechanisms of Lithium Lanthanum Titanate

Journal of The Electrochemical Society, 2023 **170** 060509

Electrochemical Stability Window and Electrolyte Breakdown Mechanisms of Lithium Lanthanum Titanate

Joseph Ring,[1] Lisa Laa,[1] Andreas Limbeck,[1] Vedran Vonk,[2] Sergey Volkov,[3] Andreas Nenning,[1,z] and Jürgen Fleig[1]

[1]*TU Wien, Institute of Chemical Technologies and Analytics, Getreidemarkt 9/164-EC, Vienna, Austria*
[2]*Center for X-ray and Nanoscience -CXNS, Deutsches Elektronen-Synchrotron DESY, Germany*
[3]*Deutsches Elektronen-Synchrotron DESY, Germany*

Perovskite-type $La_{0.57}Li_{0.29}TiO_3$ (LLTO) is a promising solid electrolyte material with high Li-ion conductivity. However, its experimental electrochemical stability window is not precisely known, and thus the compatibility with potential electrode materials is partly unclear. In this contribution, we present results from electrochemical and analytical experiments to elucidate the stability of LLTO when being polarized with Li-ion-blocking Pt electrodes. Above 2.5 V, a darkened color front starts moving from the cathode to the anode, leading to electrolyte degradation. While first-principles calculations predict the appearance of new phases as decomposition products, we find zones with modified defect chemical properties originating from the anode and cathode. The darkened zone forming at the cathode contains Ti^{3+} polarons with high mobility, which leads to a mixed ion-electron conductivity, already for a very small Li excess concentration. Next to the anode a spatially very confined, weakly conductive Li depletion zone forms. The spatially confined but substantial Li depletion near the anode could be quantified by analytical laser ablation inductively coupled plasma mass spectrometry (LA-ICP-MS). In contrast to first-principles calculations, no new phases were found near the anode, according to synchrotron-based grazing incidence XRD measurements.
 [DOI: 10.1149/1945-7111/acd818]

Manuscript submitted February 16, 2023; revised manuscript received May 12, 2023. Published June 5, 2023.

Lithium lanthanum titanate (LLTO) exhibits high bulk Li-ion conductivity at room temperature in the range of almost 10^{-3} S cm^{-1} [1–6] and reasonably low electronic conductivity $<10^{-9}$ S cm^{-1} [7] for application as an electrolyte in solid state Li-ion batteries. It has a nearly cubic perovskite-type unit cell with weak tetragonal distortion and pronounced A-site cation disorder.[8–12] The A-sites are partially occupied by Li^+, La^{3+}, and vacancies. The average charge of the A-site cations must be 2+, so the general A-site occupancy in LLTO is $La_{0.666-x}Li_{3x}TiO_3$, which yields 0.333–2× A-site vacancies per formula unit.[13,14] Around the stoichiometry of x = 0.1 (i.e. $Li_{0.29}La_{0.57}TiO_3$), the structure undergoes an orthorhombic (low Li content) to very weakly distorted tetragonal (high Li content) transition, where also the highest ionic conductivity is observed.[13,14]

In contrast to many other Li-ion conducting materials like thiosulfates or garnets, LLTO is usually considered chemically stable in ambient conditions and even in water. This enables application, e.g. in lithium-air batteries or lithium extraction from aqueous sources like seawater.[15,16] Nonetheless, the thermodynamically stable potential range is limited, and first-principles calculations predict an electrochemical phase stability window of 1.75–3.7 V vs Li metal.[17–19] Consequently, application of more than 2 V bias to Li-ion blocking electrodes may result in electrochemical decomposition of the electrolyte. These first-principles calculations predict O_2 evolution and formation of $La_2Ti_2O_7$ and $Li_4Ti_5O_{12}$ at the anode, whereas Li-rich phases that contain Ti^{3+}, like $Li_7Ti_{11}O_{24}$, $La_2Ti_2O_7$ and $Li_4Ti_5O_{12}$ are the most stable phases at the cathode.

The practically usable potential window may be larger, particularly when the kinetics of electrolyte decomposition is sluggish (which is expected for processes that involve the formation of new solid phases and reorganization of La, Ti and O ions at room temperature). On the other hand, the Li chemical potential in an electrolyte is directly proportional to changes of the Fermi level within the bandgap. Therefore, electron or electron hole concentrations are functions of the Li chemical potential within the thermodynamic stability window. Too high electron or hole concentration may lead to a breakdown of the electrolytic domain when the ionic transference number drops significantly below one. Noteworthy, Li ion conductors typically have localized polaronic electron and hole defects, which have energy levels inside the band gap, so the stoichiometry stability window is somewhat smaller than the band gap. Recent computational studies of these polaronic energy levels predicted a reductive stability limit of 1.5–1.7 V vs Li^0, and an oxidative stability limit of 4.5–5.3 V, depending on the used DFT potentials.[20] Given these significant computational uncertainties regarding the stability limits and breakdown mechanisms, experimental studies are required to determine the practically usable Li potential range for LLTO electrolytes. Some discrepancies between thermodynamic calculations and experimental data are already known. For example, it is experimentally known that LLTO does not decompose when subjected to Li potentials lower than 1.7 V vs Li but rather reversibly inserts Li into vacant A-sites[21–23] or even interstitial 3c sites at potentials lower than 1.2 V vs Li metal.[22,24] Due to the charge compensation by conduction band electrons, the material becomes a mixed ionic electronic conductor (MIEC). It behaves then more like an electrode material than as an electrolyte, and indeed LLTO may be usable as an anode material with high C-rate and cycling performance.[24] During Li insertion, charge neutrality is preserved primarily by reducing Ti^{4+} to Ti^{3+} since the conduction band of LLTO has a predominant Ti-3d character. This was experimentally confirmed upon reduction of LLTO via in situ XPS.[25] Accordingly, LLTO does not undergo phase decomposition below 1.7 V but is disabled as an electrolyte since it becomes an electronic conductor, as predicted computationally in Ref. 20. Recent investigations of the reduction of LLTO even indicate that the ionic transference number of LLTO drops below 0.99 already at 2 V vs Li metal.[23] The oxidative stability limit of LLTO is, however, less investigated. It was demonstrated that surface coating with a thin LLTO layer could improve the stability of the cathode material $LiNi_{0.8}Co_{0.15}Al_{0.05}O_2$,[26] or $LiNi_{0.83}Co_{0.12}Mn_{0.05}O_2$[27] by enhancing cycling performance and charge transfer kinetics at potentials up to at least 4.2 V vs Li^0. This suggests that the operational oxidative stability window is larger than the phase decomposition calculations indicate.

In this study, electrochemical experiments are performed on LLTO polycrystals with Li-ion-blocking Pt electrodes to investigate the electrochemical phenomena taking place under voltage load, to

[z]E-mail: andreas.nenning@tuwien.ac.at

determine the practical electrochemical stability limits and to explore the reactions taking place in/at LLTO when exceeding these limits.

Electrolyte degradation reactions are especially critical when the degradation product is either a good electron conductor or a very bad Li ion conductor. In the former case, self-discharge through electrical short circuiting will occur, while the latter case will lead to substantial deterioration of the rate capability. CV measurements that are often employed allow for a quick estimation of the stability window. However, they yield no information on the mechanism of the electrolyte breakdown, which is why we employed additional characterization methods. Moreover, sluggish decomposition reactions with correspondingly low current may lead to an overestimation of the stability window in CV measurements. In the case of cubic garnet-type LLZO, stability windows up to +9 V vs Li^0 are reported based on CV[28] measurements on pellets, while cycling of LLZO powder[29] in liquid electrolyte and accelerated degradation at elevated temperature[30] showed that oxidative degradation already starts slightly above 4 V.

The breakdown mechanism next to the negatively polarized cathode was investigated primarily by observing an electrocoloration front under DC load, and spatially resolved Li activity and conductivity measurements. The spatially more confined Li depletion next to the positive anode was more closely investigated by synchrotron XRD studies, and laser ablation inductively coupled plasma mass spectroscopy (LA-ICP-MS) for measuring changes in the local Li stoichiometry induced by DC bias. It is shown that a very strongly Li-depleted zone is formed directly under the anode, while at the cathode, a spatially extended but only slightly Li-enhanced colored region develops.

Experimental

A large polycrystalline LLTO-sheet (0.5 mm thick) with nominal stoichiometry $La_{0.57}Li_{0.29}TiO_3$ was used for sample preparation (Toho Titanium Co., Ltd., Japan). Rectangular samples, with typical dimensions of 5 × 12 mm2, were prepared by cleaving. Li-blocking Pt electrodes (for experiments type I—III) and Au electrodes for experiment type IV (200 nm thick) were deposited onto the sample surface by magnetron sputtering (Baltec Med 020) at room temperature and patterned by an alumina shadow-mask. Potentiostatic field-stress was applied to samples using platinum needles and a Keithley 2611B Source-Meter-Unit, which was also used to measure open circuit voltages (OCVs). Different sample and electrode geometries were employed in various types of experiments. This is sketched in Fig. 1. In experiment type I, voltages of 1–20 V were applied between stripe electrodes (ca. 2 mm wide) and time-dependent currents as well as appearance and movement of a color front were measured. In experiment type II (see Fig. 1), the voltage was applied between an extended counter electrode and a small circular working electrode (800 μm in diameter). After polarization for 4, 20 and 52 min, the external load was removed and the OCV was measured between the working electrode and another small circular electrode at some distance. Moreover, impedance spectra were measured with a Novocontrol Alpha-A High Performance Frequency Analyzer (Novocontrol Technologies GmbH & Co. KG, Germany), between several electrode pairs to get information on the corresponding local conductivity. This coloration and characterization sequence was reported several times. Both types of experiments were conducted in an evacuated ($p<10^{-5}$ mbar) sample chamber at room temperature, unless otherwise described.

The local chemical composition of LLTO after voltage load was measured by laser ablation inductively coupled plasma mass spectrometry (LA-ICP-MS). An excimer-based laser ablation system (ESL193, Elemental Scientific Lasers, United States) was used which utilizes argon, fluorine and helium (buffer gas) as laser medium and operates at a wavelength of 193 nm in the UV range. Laser pulses with durations of few nanoseconds were produced by this LA instrument. The laser was controlled via the software "Active View 2," which had been delivered together with the instrument. As an ablation chamber an analytical cup (TwoVol2, Elemental Scientific, United States) was used. As ICP-MS device (iCAP Q, ThermoFisher Scientific, Germany) equipped with a quadrupole mass analyzer was employed. The data evaluation was conducted by the software "Qtegra." The connection between the LA device and the ICP-MS instrument was achieved by using a polymeric tube (Tygon®, inner diameter: 1.6 mm) and a dual concentric injector (DCI, Elemental Scientific, United States). All operating parameters are summarized in Table I. In the corresponding experiment type III two circular electrodes (1 mm diameter) were sputtered on small (ca. 2 × 6 mm^2) LLTO sheets and polarized in vacuum (10^{-5} mbar) at 100 °C–150 °C. Samples were polarized at 4–8 V for up to 90 min LAMS measurements were performed ex situ after polarization (see sketch in Fig. 1).

Experiment type IV was performed at the synchrotron DESY, beamline P08.[31] Therein, a highly collimated (30 × 30 μm) X-ray spot with 11.8 keV was focused on a gold electrode in shallow incidence (5° angle of incidence) mode, which results in a mean X-ray penetration depth of 2 μm relative to the surface normal. Diffraction patterns were collected by movement of a 2-D detector (Pilatus100K, 195 × 487 pixels) along the Θ axis at constant angle of incidence. The detector was moved along the Θ-axis, and multiple detector snapshots were stitched together to generate 1-D and 2-D diffractograms.

Results

Electrocoloration of LLTO.—In experiments of type I (cf. sketch in Fig. 1), LLTO sheets with Li-ion blocking Pt electrodes were subjected to a DC voltage at room temperature inside a vacuum chamber with a base pressure of 10^{-5} mbar. Since voltage and current have the same sign in our experiment, the cathode is the negative and the anode is the positive electrode. The onset of electrolyte reduction is even visible optically. When the applied voltage exceeds 2.4 V, a colored zone appears at the cathode and propagates toward the anode. The intensity of the coloration and its velocity increase with voltage. As an example, the movement of a color front is shown in Figs. 2a–2d for an applied potential of 5 V; the corresponding current is given in Fig. 2f. The velocity of the color front decreases with time, as can be seen by the time-dependent location of the color front plotted in Fig. 2f. However, such coloration in LLTO is only observed in an oxygen-, CO_2- and moisture-free environment like a glove box or vacuum chamber pumped by a turbo molecular pump. Once a colorized sample is exposed to air, the color disappears (see Fig. 2e). In contrast to electrocoloration experiments on the chemically similar perovskite $SrTiO_3$,[32] no color front is visible next to the anode. Instead, the cathodic color front appears to reach the anode of the sample. The absence of an anodic coloration front may either stem from a strongly confined Li depletion zone, or Li depletion without visible color changes. Type III and IV experiments in Fig. 1 deal with the properties of this anodic zone. Please note that we used the terms "anode" and "cathode" in the common electrochemical definitions, i.e. representing an oxidation reaction at the positive anode or a reduction at the negative cathode electrode. In terms of Li chemical potential, the cathode is thus much closer to Li metal than the anode.

The electrical characteristics of experiments with voltages from 1 to 20 V are shown in Fig. 3a. The gap in the 20 V curve around 50 s is due to a short loss of contact which however does not impede the qualitative discussion. The noise at the end of the 1 V measurement stems from the very low current in the 10^{-10} A range. Figure 3b displays the voltage-dependent currents after 100 and 300 seconds, respectively. Already between 1 V and 2 V, we find a strongly non-linear increase of the current. However, from 2 to 3 V the current increase is very pronounced (factor of 27 at 100 s), suggesting that something changes qualitatively at such voltages, and indeed this is the voltage range where the visible color front appears. Moreover, at high voltages, we find a current minimum after some time, and this

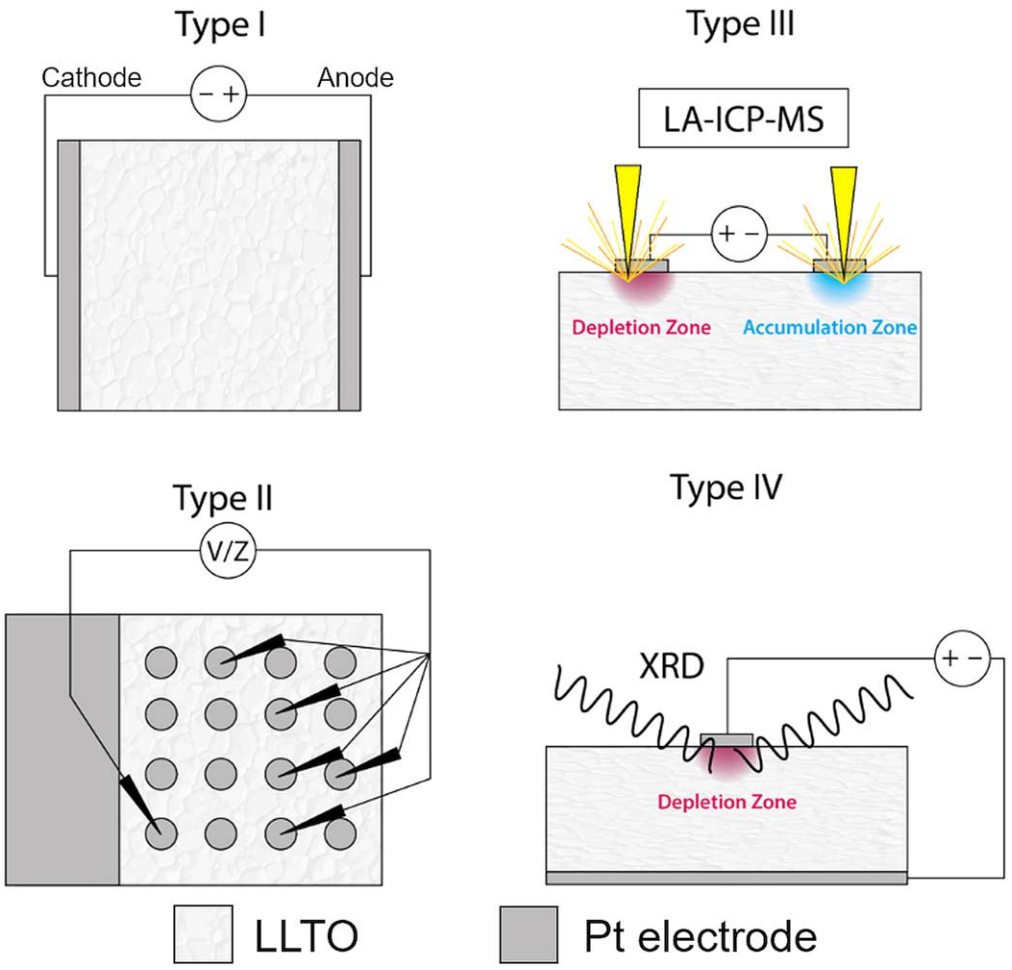

Figure 1. Schematics of experimental setups: 2-electrode electrocoloration (Type I), recording current over time; multiple electrode coloration (Type II) where OCVs and impedance spectra of multiple electrodes were measured repeatedly alongside electrocoloration; LA-ICP-MS depth profiles of field-stressed LLTO samples (Type III) and in situ micro focused XRD (Type IV).

Table I. Operating parameters of the LA- and ICP-MS instrument.

Laser ablation	
Laser fluence	1.25 J cm^{-2}
Beam size	20 μm
Repetition rate	100 Hz
Overlap	10 μm
Scan speed	1 000 μm s^{-1}
He flow	800 ml min^{-1}
Inductively coupled plasma mass spectrometry	
RF power	1 550 W
Auxiliary gas flow	0.80 ml min^{-1}
Cool gas flow	14.0 ml min^{-1}
Nebulizer gas flow	0.72 l min^{-1}
Dwell time per mass	10 ms
Measured Isotopes	^{6}Li, ^{46}Ti, ^{138}La

minimum coincides with the time needed by the visible color front to pass the entire sample and reach the anode. The different durations to reach a minimum (5 V: 2700 s, 20 V: 520 s, see Fig. 3a) also show that the velocity of the color front increases with voltage.

When we assume that the current in the uncolored zone of the LLTO sheet is primarily ionic, we may calculate the amount of Li-ions accumulated in the reduced zone (and thus removed from the oxidized zone). By dividing the number of transported Li ions through the number of ABO_3 units in the colored zone we can determine the Li excess stoichiometry in $La_{0.57}Li_{0.29+\delta}TiO_3$ in the colored zone according to

$$\Delta c(Li^{+})_{color} = \frac{V_m}{FV_{color}} \int_{t=0}^{t_x} I_{DC}\, dt. \quad [1]$$

Therein, F is Faraday's constant, V_m is the molar volume of LLTO (35.1 cm^3), V_{color} is the volume of the colored zone (colored area times thickness of the sheet) and t_x is the polarization time at which the volume of the colored zone is determined. The values of this calculation are summarized in Table II. The relation of colored LLTO volume vs charge is given in Fig. 4, where we observe a nicely linear trend at 5 V and 20 V, and a comparatively large and less dark (not shown) colored volume for the 3 V experiment. Noteworthy, for all data points in Fig. 4 the Li overstoichiometry in the colorized zone is consistently below 10^{-4} per formula unit (p.f.u) - much less than the concentration of vacant A-sites (0.14 p.f.u.). The charge of these additional Li-ions is compensated by the reduction of Ti^{4+} to Ti^{3+}, and this introduces mixed ion and electron conductivity as already suggested by previous studies on the electrochemical and thermal reduction of LLTO.[25,33] The high velocity of the coloration front propagation indicates high mobility of these electronic carriers, which was recently confirmed by conductivity measurements on electrochemically reduced LLTO sheets.[23]

Localized Li activity measurements.—To further investigate the mechanism and driving forces of the electrocoloration, multiple

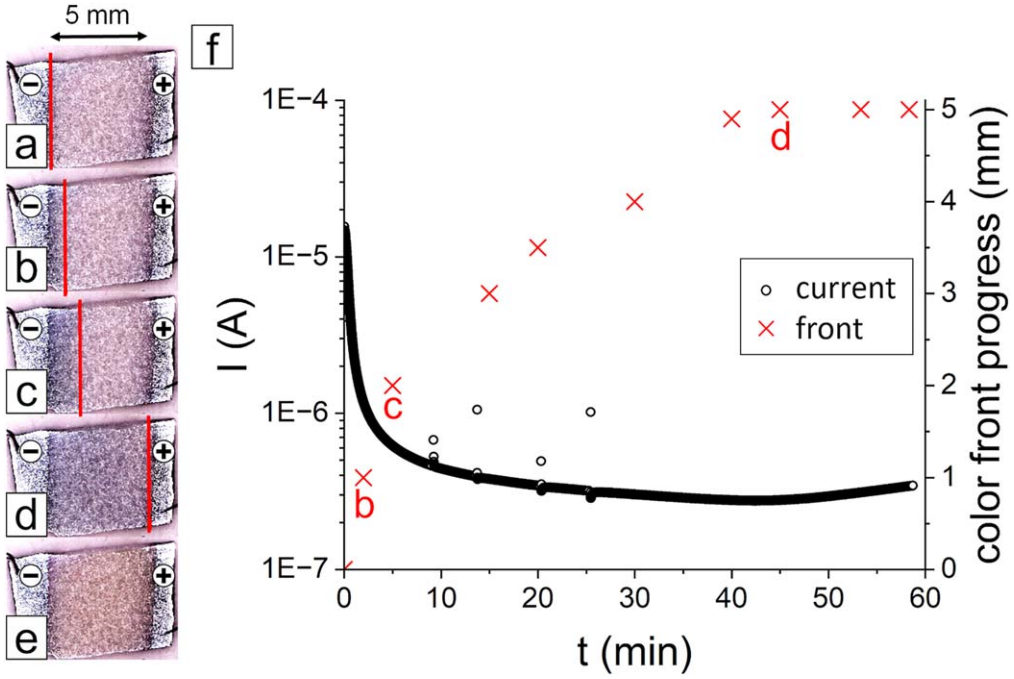

Figure 2. Photographs of the LLTO sample before (a) and during (b)–(d) an electrocoloration at 5 V. The color front progress is indicated by vertical red lines. After 60 min, air was introduced to the sample chamber (e). Panel (f) shows the current over time (black circles, left axis) and the progression of the coloration front (red crosses, right axis), with times corresponding to (b)–(d) marked by red letters.

small electrodes were used in experiment type II (see sketch in Fig. 1 and photograph in Fig. 5a). During the experiment, a constant voltage of −5 V was applied between a large rectangular anode, labelled counter electrode (CE) in Fig. 5a, and a ⌀ 850 μm circular cathode (working electrode, WE). In this configuration, the coloration front propagates almost concentrically around the negative circular cathode. The bias load was paused after several minutes and open circuit voltages (OCVs) were measured between various circular electrodes and a reference electrode (RE) outside the colored zone. Then, the electrocoloration process was continued. This procedure was repeated before polarization, and after 4, 20 and 52 min, shown in Figs. 5c–5f.

Impedance spectra were measured between different circular electrodes before and after coloration, shown in Fig. 5b to measure conductivity changes during electrocoloration. These exhibit an incomplete high-frequency feature, an x-axis intercept resistance (R_{hf}) at ca 25 kΩ, and a low-frequency feature that is associated with the ion blocking electrodes. The axes intercept R_{hf} is roughly twice the spreading resistance of a single electrode, so we can calculate the conductivity of LLTO from the real axis intercept according to $\sigma_{ion} = (R_{hf}\, d_{el})^{-1}$, where d_{el} is the electrode diameter (0.85 mm) The value of roughly $5*10^{-4}$ S cm^{-1} is in line with the manufacturer's statement and own measurements on sheets with macroscopic coplanar electrodes (not shown). Remarkably, this resistance does not change after coloration, indicating that the total conductivity remains the same and any electronic conductivity introduced by the coloration is significantly lower than the ionic conductivity. A virtually unchanged ionic conductivity during overlithiation is also in accordance with literature.[21] At low frequencies, the impedance spectra are characterized by electrode features. Those show some changes during coloration but their mechanistic discussion is out of the scope of this paper. Figures 5c to 5f show the OCVs of individual electrodes relative to the RE. For these measurements, the bias was lifted from the CE and voltages vs the RE (green in Fig. 5a) were measured. This OCV reflects the Li chemical potential difference between the investigated electrodes. Before any DC voltage was applied, the voltages between the different circular electrodes and the reference electrode were in the 10 to 20 mV range, which indicates that the sample was chemically equilibrated. After 4 min the working electrode reached 2.4 V, while all other electrodes were still close to zero. All neighboring electrodes were above 2 V after 20 min and later (after 95 min) those electrodes are essentially equipotential at 2.4 V. Noteworthy also a voltage of 2.5 V marks the onset of a weak cathodic coloration. The measured equally low electrode potential exclusively within the colored zone indicates that some degree of electron conductivity is present in the colorized zone.

Stoichiometry and structure of the Li-depleted zone.—In contrast to the cathodic coloration zone, the Li depletion next to the anode is not optically visible. This suggests that it is spatially strongly confined to a volume directly underneath the anodic terminal. To validate this hypothesis, laser ablation inductively coupled plasma mass spectroscopy (LA-ICP-MS) was employed to determine the chemical composition in localized zones of the LLTO samples: a focused laser with a beam size of 20 μm was used to remove material. By appropriate laser parameters and calibration standards (see Experimental), Li stoichiometry quantification with a depth resolution of about 100 nanometers could be achieved.

Reference experiments on pristine samples showed that within < 1 h after grinding or ultrasonic cleaning in H_2O, the surface gets Li-enriched. Most likely, this is due to Li_2CO_3 or LiOH, formed by a topotactic Li^+/H^+ exchange reaction triggered by humidity and CO_2 in the ambient atmosphere, as shown in Ref. 34 for LLTO and Ref. 35 for garnet-type LLZO. Surface Li enrichment is even present after >1 week of storage in a desiccator. The surface enrichment of Li decreases the accuracy of quantitative comparison of the Li content in LLTO before and after polarization. To enhance the amount of Li depletion in the anodic depletion zone, we increased temperature during polarization to 150 °C. Figure 6a shows that a strong coloration front around the cathode is visible under these conditions.

In Fig. 6b, Li depth profiles in the depleted zone beneath the anode are shown after 80 min of polarization at 150 °C using voltages of 4, 6 and 8 V. Already for 4 V, a very strong Li depletion by more than 50% is found in the first few 100 nm; the Li content increases with depth and reaches the bulk value in about 4 μm depth.

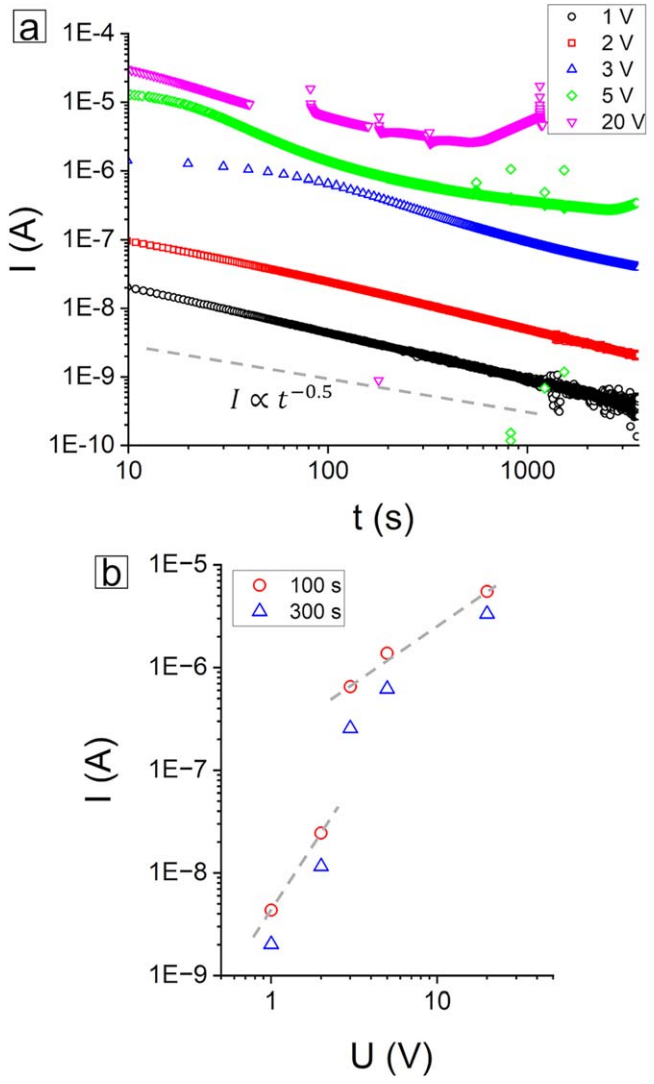

Figure 3. (a) Current over time of various electrocoloration experiments. The dashed line indicates the slope of $I \propto T^{-0.5}$. (b) Measured DC current after 100 s (red circles) and 300 s (blue triangles) as a function of the applied DC voltage. The grey dashed lines are a guide for the eye to illustrate the steep current increase from 2 to 3 V.

Table II. Experimental data from polarizations with 1–20 V, including the estimated coloration zone volumes and corresponding Li excess, calculated via integration of current over time.

U (V)	t (s)	Q (C)	V_{color} (mm^3)	ΔcLi^+_{color} (p.f.u.)
1	300	$1.6*10^{-6}$	0	no coloration
2	300	$8.2*10^{-6}$	0	no coloration
3	300	$1.8*10^{-4}$	1.6	$4.4*10^{-5}$
5	300	$6.3*10^{-4}$	2.9	$8.4*10^{-5}$
20	300	$1*10^{-3}$	8.0	$8.3*10^{-5}$

For 6 V, the situation is even more pronounced, with almost complete Li depletion up to ca. 2.5 μm, followed by an increase to the bulk value at ca. 6 μm. For 8 V, an almost complete Li depletion is detected in the entire depth measured, i.e. to 9 μm. These measurements showed that, indeed the zone beneath the anode shows very strong Li depletion and is confined to a rather thin layer. For room temperature measurements and thus much lower currents than used in this type IV experiments we may expect Li depletion

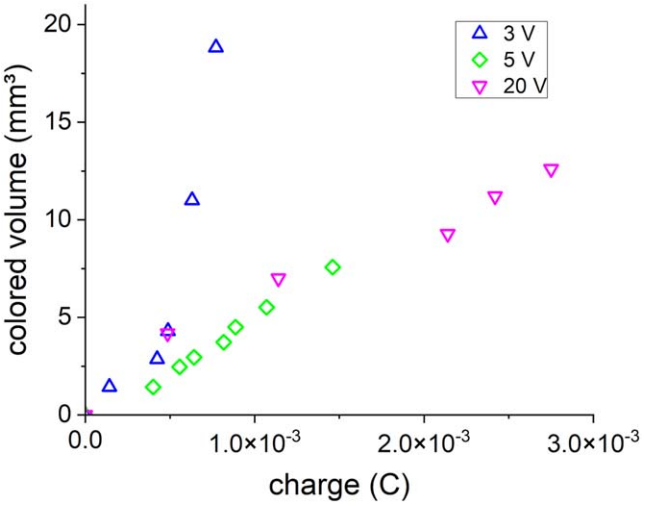

Figure 4. Accumulated charges (calculated by integration of currents over time) and corresponding volumes of the colored zones from electrocoloration experiments at 3 V (blue triangles), 5 V (green diamonds) and 20 V (pink triangles).

layers in the μm range. Furthermore we can calculate the cumulative charge of the depleted Li-ions by

$$Q_{dep} = \frac{FA_{el}}{V_m} \int 0.29 - c(Li^+)dz. \quad [2]$$

Therein, V_M is the molar volume of LLTO (37.5 cm^3/mol), and A_{el} is the area of the anodic electrode, F is Faraday's constant and $c(Li^+)$ is the measured Li stoichiometry per formula unit and z is the ablation depth. The calculated charges are $4*10^{-4}$ C for 4 V, $1.4*10^{-3}$ C for 6 V and $>3*10^{-3}$ C for 8 V. These values are roughly twice the electrically measured charge, indicating that the current is partly also electronic under these conditions.

To get more insight into the structure of the Li-depleted zone at the anode, in situ synchrotron XRD measurements were performed (experiment type IV). Therein, a sample of LLTO (cut from the 0.5 mm thick sheet) was subjected to oxidative field stress (up to 7 V) with a small working electrode (Au, 0.6 mm^2) and a larger counter electrode (Au, 10 mm^2) in a cross-plane geometry at 25 °C for several hours.

In Fig. 7, the XRD results are summarized. Due to the small X-ray spot size, only a few crystallites randomly produce reflexes, rather than Debye–Scherrer rings, as shown in the 2-d diffractograms in Figs. 7c–7d. Therefore, the peak intensities in the integrated scans are stochastic, and a Rietveld refinement is impossible. The reflexes were indexed according to the tetragonal unit cell with a size of 1 × 1 × 2 cubic perovskite unit cells, with a = b = 3.867 Å; c = 7.781 Å, according to Ref. 36. The corresponding theoretical reflex positions are marked by vertical lines. Upon application of anodic bias up to 7 V, no new crystalline phases were found during field stress, even with a bright Synchrotron X-ray source. The formation of amorphous phases cannot be excluded. However, since the total integrated intensity of the diffraction patterns does not change significantly, we rule out that a thick (>1 μm) amorphous layer has formed. The peak splitting of the LLTO reflexes becomes more pronounced and complex with bias, as shown in Fig. 7. This indicates that the tetragonal distortion of the unit cell increases significantly. It is expected that the lattice distortion changes when point defect concentrations change (e.g. more Li vacancies). The XRD measurements show that the Li-depleted zone consists (at least partly) of Li-depleted LLTO. It is, however, likely that stoichiometry and structure change along the sampling depth and potentially between different grains, so a reliable quantification of the structural distortion is not possible.

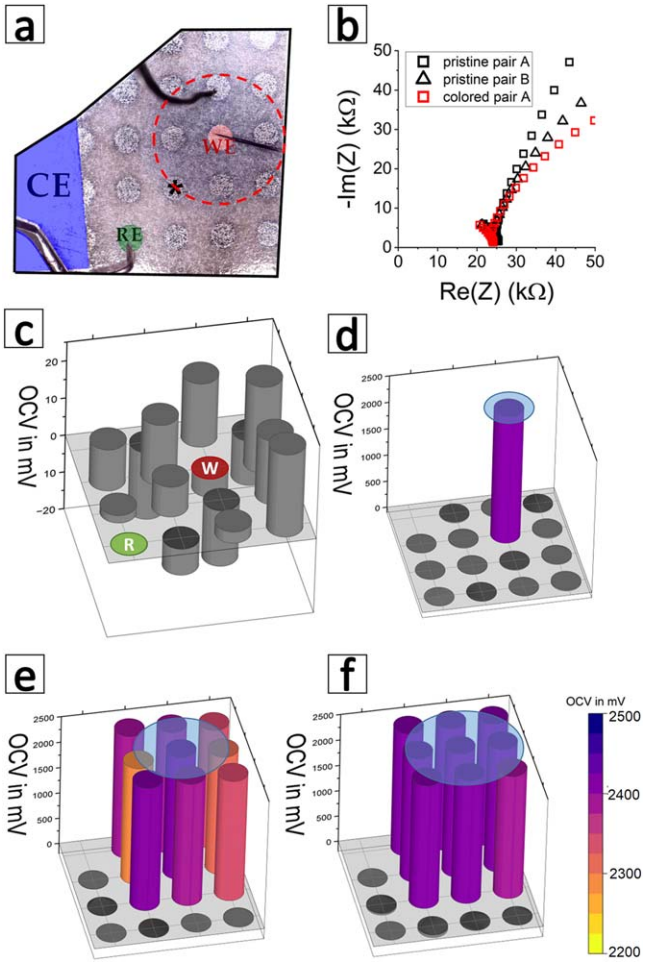

Figure 5. Electrocoloration experiment with multiple electrodes. (a) Photograph of the colorized LLTO sheet after 52 min polarization. (b) Impedance spectra of neighboring circular electrode pairs prior to coloration (Black squares and triangles) and after (red squares) coloration for 52 min (both electrodes were in the colored zone). The electrode pair "A" is marked by (*) and (WE) in panel (a). (c) shows the OCVs of various circular electrodes versus the RE (marked green in panel a). Parts (d)–(f) show the development of OCVs throughout the coloration experiment after 4 min (d) 20 min (e) and 52 min (f) voltage application. The progression of the coloration front is sketched as a blue overlay.

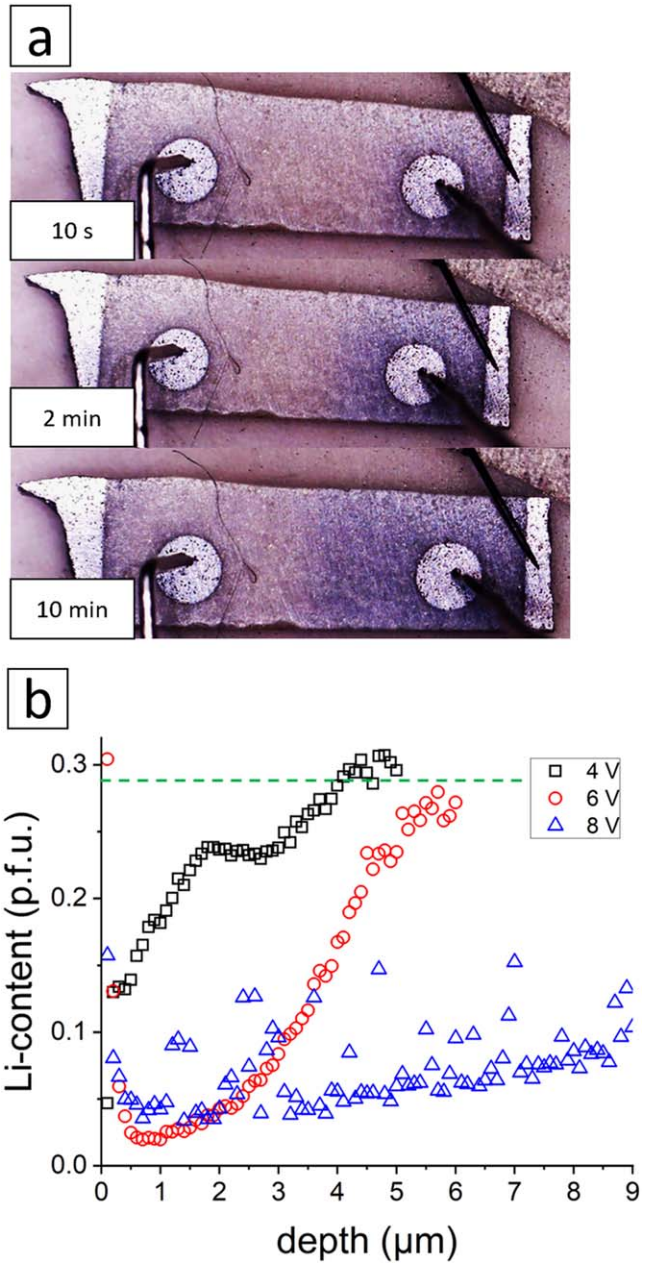

Figure 6. (a) Photographs of an LLTO sheet during coloration. (b) shows the Li-concentration depth-profiles of anodes, polarized with 4 V (black squares), 6 V (red circles) and 8 V (blue triangles) at 150 °C for 80 min, respectively.

Discussion

Mechanism and thermodynamic driving forces for LLTO coloration.—DC polarization of mixed conducting materials with blocked majority charge carriers leads to a so-called stoichiometry polarization.[37,38] In the case of a predominantly ion-conducting material with blocked ion transport at the electrodes, a redistribution of ions takes place with Li depletion next to the anode and accumulation next to the cathode. For voltages within the stability limit, these are compensated by concentration changes of electron and electron-hole charge carriers, or by filling and depleting deep trap states within the band gap. The case of two blocking electrodes this was described by Yokota or Miyatani,[39,40] while for one reversible and one blocking electrode we refer to it as Hebb-Wagner experiments.[41–43] In such measurements the ionic current decreases towards zero and finally only the electronic current remains. However, the concentrations of electrons and holes are very low within the stability limit of 2.5 V, so also the current density constantly decreases with no corresponding coloration, as seen in Fig. 3. Higher voltages, particularly above the electrochemical stability window, lead to further decomposition processes, which are in our study's focus. First, we consider the extended coloration front that emerges from the cathode, which is related to Li accumulation (as in a Hebb-Wagner experiment).

A strong darkening of LLTO and rise of electronic conductivity were reported in literature after reductive sintering[33] or electrochemical lithiation through an organic electrolyte with an external Li source.[21] Also during electrocoloration, Li is introduced into vacant A-sites, while the charge is balanced by the reduction of Ti^{4+} to Ti^{3+}. Accordingly, instead of decomposition and formation of new phases, a certain Li-excess stoichiometry arises, also under high voltages. As a result, significant electron conduction can be expected in this zone, particularly due to the reported high electron mobility in reduced LLTO.[33] Still, the impedance measurements showed that the electronic transference number remains comparatively small in the colored zone. Mixed conductivity in the colorized region also explains the observation that in type II experiments electrodes within the colored region have almost zero voltage relative to the cathode,

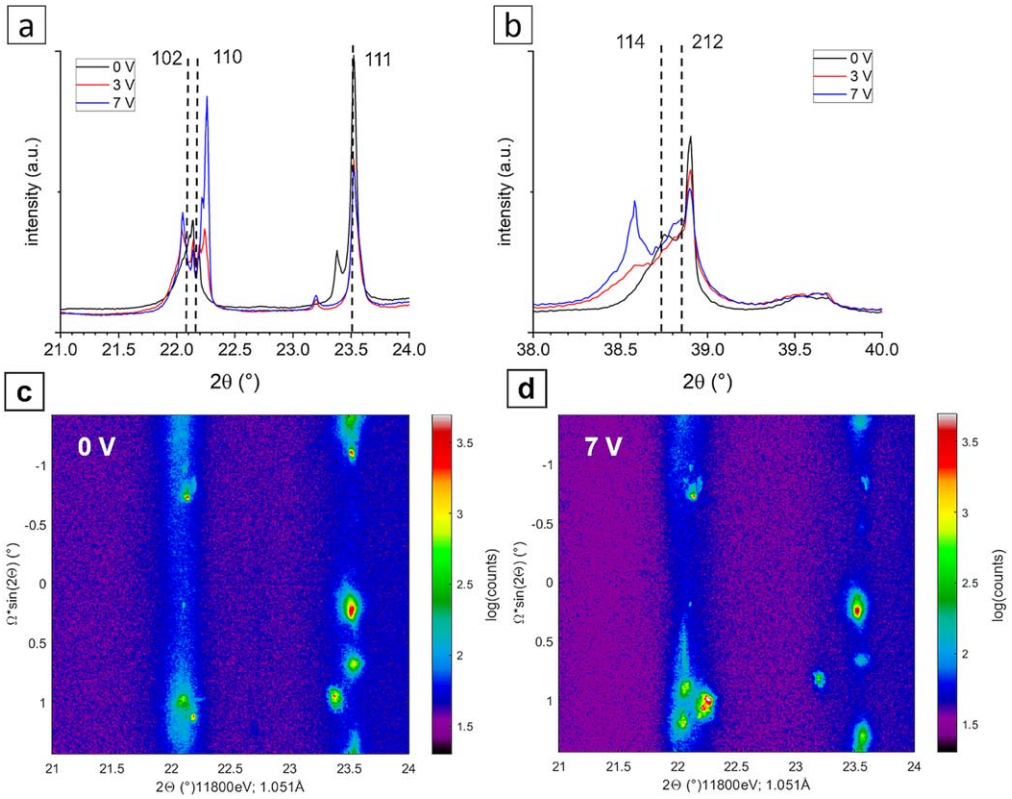

Figure 7. Exemplary diffractograms from in situ synchrotron XRD measurements. The intensities of all diffractograms were normalized to the integral of the Au (111)-reflex at about 26° (originating from the electrode), not shown here. (a) (110)/(102) (22.3°) and (111) -reflexes (23.5°), (b) (212)/(11 4)-reflexes at 39°. All reflexes split further apart with increasing potential, indicating an increasing lattice distortion from the ideally cubic perovskite structure. Plots (c) and (d) show the 2-d diffractograms in the 21–21° range, which exhibit only a small number of crystallites that produce sharp reflexes.

whereas they remain close to the anode potential in the uncolored region, which therefore remains as intact electrolyte. This proves that not only the color but also the Li chemical potential gradient is rather steep outside the colored zone. From the integrated charge and unchanged ionic conductivity in the colored zone, we conclude that the Li vacancy concentration is hardly changed (overstoichiometry of $<10^{-4}$ p.f.u.) and thus the chemical potential of Li ions (μ_{Li+}) is almost constant. Changes of the lithium chemical potential, given by $\mu_{Li} = \mu_{Li^+} + \mu_{e^-}$, are directly linked to the electron chemical potential μ_{e^-}, or Fermi level. Consequently, the onset of coloration of LLTO corresponds to the Fermi level at which Ti^{4+} gets partly reduced to Ti^{3+}, which is close to the conduction band edge. According to an experimental study by Birke et al. [21] this process happens in the Li potential range of 1.7–1.8 V vs Li metal, and own measurements even suggest the onset of electron conductivity at 2 V Vs Li metal.[23]

The coloration vanishes quickly in presence of O_2, CO_2 and water vapor. The standard equilibrium voltage for the formation of Li_2O_2 is 2.9 V vs Li metal. The Li chemical potential in the colorized LLTO corresponds to 1.7–2 V vs Li metal, which is significantly below the typical discharge potential of Li-air batteries.[44] The discoloration occurs by a redox reaction in which Ti^{3+} is oxidized and O_2 gets reduced, according to

$$2\,Li^+ + 2\,Ti^{3+} + O_2 \rightarrow 2Ti^{4+} + Li_2O_2. \qquad [3]$$

The Gibbs energy decrease of this reaction is roughly 1 eV per Li ion. Owing to fast chemical diffusion of Li—which is similar to the color front propagation speed - this reaction may thus take place at the surface at a rate that is sufficient for fast discoloration. Humidity and CO_2 may further lead to conversion of Li_2O_2 to LiOH and Li_2CO_3. This reaction is different to the Li surface enrichment on unpolarized LLTO. There, a comparatively sluggish topotactic Li^+/H^+ exchange leads to formation of Li-rich surface phases.[34]

Although the electrolyte degradation is only visible in form of a cathodic coloration front, the reactions occurring next to the anode are limiting the degradation kinetics. When a voltage of 5 V is applied to LLTO, the OCV between anode and cathode remains at about 2.4 V after switching off the external voltage source. The rest of the applied voltage of roughly 2.6 V must therefore be a kinetic overpotential that is associated withion conduction in the LLTO sheet and electrochemical reactions near the cathode and the anode. This raises the questions of origin and location of such a large kinetic overpotential in polarized LLTO. In experiment type I, the current density at 5 V is less than about $5*10^{-4}$ A cm^{-2} after 10 s and decreases to less than $3*10^{-5}$ A cm^{-2} after 200 s. With a total conductivity in the range of $5*10^{-4}$ S cm^{-1} we can thus estimate the ohmic overpotential across the bulk part of the sample as about 1 V (10 s) and <60 mV (>200 s)—meaning that only a small fraction of the kinetic overpotential is due to ion conduction.

Hence, the majority of the kinetic overpotential (2.6 V) has to be consumed by a process in the anode-near Li depletion zone. Moreover, the kinetics of the anodic Li depletion process decrease significantly with time, and the decay rate of the current resembles (although not perfectly) a diffusion-limited process. The growth rate of the colorized zone, shown in Fig. 2, also resembles a diffusion-limited process. However, Ti^{3+} ions can only increase but not decrease the conductivity in this region, which would lead to current rising with time.[32] Consequently, the major part of the kinetic overpotential is associated with the Li depletion reaction at the anode rather than over lithiation at the cathode.

Chemical and structural changes in the Li depleted zone.—The largest part of the kinetic overpotential is confined to a rather narrow, heavily Li-depleted zone at the anode. The LA-ICP-MS results after polarization at 150 °C revealed depletion zones in the μm-range. For the room temperature experiments, we can estimate the Li depletion

thickness from the integrated electrical charge, which corresponds to the number of depleted Li ions under the anode. Assuming that roughly 0.15 li atoms are missing per unit cell, we can calculate the Li depletion depth. After polarization with 5 V for 5 min at room temperature, the charge of $6*10^{-4}$ C (see Table II) corresponds to a Li depletion thickness of 0.8 μm. In this case, the kinetic overpotential is in the range of 2.5 V and the total current is $5*10^{-7}$ A. A homogeneous electric field in the Li depleted zone is thus as large as 30 kV cm^{-1}, provided the rate limiting conduction process takes place in this zone. This corresponds to a rather low conductivity of about $4*10^{-10}$ S cm^{-1}. Interestingly, this value is within the (admittedly rather large) error when extrapolating the oxide ion conductivity of slightly oxygen deficient $SrTiO_3$ from Ref. 45 to room temperature. Based on the observed strongly confined Li depletion and the calculated low conductivity in the depleted zone, we now discuss the type and mechanism of this oxidation reaction at the anode. The Li-ion depletion requires the appearance of a relative positive counter charge. We consider three mechanisms or anodic reactions that may establish the required charge balancing, see sketch in Fig. 8.

The first possible mechanism sketched in Fig. 8a is simply Li stoichiometry polarization, with electron holes as charge balancing point defect—corresponding to an electron chemical potential that approaches the valence band maximum. This happens e.g. in layered oxide cathodes. However, a significant electron hole concentration should also induce significant electron hole conduction in the Li-depleted zone. This would in turn lead to a more diffuse depletion zone, which builds up with low kinetic overpotential—similar to the near-cathode reduction. This obviously contradicts our observations. Hence, we think that this mechanism may be present for voltages below 2.5 V (at least to a certain extent) but does not dominate the electrocoloration phase at voltages above the stability limit. Please note: This (reversible) Li depletion with hole charge balancing by electron holes is not a true decomposition and does not limit the electrochemical stability in terms of decomposition, though it may certainly limit the applicability of the electrolyte due to electron conduction.

However, also when the Fermi level remains well within the band gap, the Li chemical potential is closely linked to the oxygen chemical potential, due to the relations

$$\mu_{Li} = \mu_{Li^+} + \mu_{e^-} \quad [4]$$

and

$$\mu_{O_2} = 2\mu_{O^{2-}} - 4\mu_{e^-} \quad [5]$$

In electrolytes, the Li-*ion* chemical potential is virtually constant, as the concentrations of occupied and vacant Li sites are virtually constant. Hence, changes of the Li chemical potential are almost entirely related to changes of the electron chemical potential (or Fermi level). Consequently, also the oxygen ion chemical potential is linked to the (neutral) Li chemical potential. According to Nernst's equation, a decrease of μ_e (which corresponds to an increase of μ_{Li}) by only 59 meV corresponds to an increase of the equivalent $p(O_2)$ by 4 orders of magnitude. It is likely that the electron chemical potential at which μ_{O2} corresponds to 1 bar, (according to Eq. 5) is considerably (some 100 meV) above the valence band maximum. When an applied voltage decreases the electron chemical potential beyond this point, there is a strong driving force for formation of oxygen gas at the LLTO surface, rather than building up a substantial electron hole concentration. The depletion of Li next to the anode is therefore best described by the following reaction equation:

$$2O_O^{\times} + 4\,Li_{Li}^{\times} \overset{-4Li^0}{\rightarrow} 2V_O^{\cdot\cdot} + 4V_{Li}^{\prime} + O_2. \quad [6]$$

This reaction is essentially Li_2O depletion in the perovskite, sketched in Fig. 8b. It is similar to the mechanism proposed for Garnet type Li conductors,[30] in which high oxygen anion mobility was observed, which indicates a considerable amount of oxygen vacancies.[46] Also, the stronger lattice distortion found at anodic bias supports this hypothesis of defect chemical changes. Further, the calculated conductivity of the Li depleted zone is in line with assuming rate limiting oxygen ion conduction. Moreover, the growth of such a weakly conductive oxidized zone would be diffusion limited, in accordance with the decaying DC current. This oxygen loss is most probably irreversible at low temperature.

The third possible mechanism (Fig. 8c) involves secondary phase formation as indicated by DFT calculations, which suggest the appearance of TiO_2, $La_2Ti_2O_7$, and O_2[17] at a voltage >3.7 V vs Li metal. Indeed, $La_2Ti_2O_7$-impurities may form in LLTO, likely due to Li-loss during synthesis.[47] However, such a phase transition would require substantial re-organisation of La, Ti and O ions which are hardly mobile at room temperature. Nonetheless, almost complete depletion of Li_2O in LLTO may cause structural instability and partial amorphisation of the Li depleted zone. This would be hardly detectable by XRD when the amorphous layer is sufficiently thin.

Model of electrocoloration and electrochemical stability of LLTO.—The reactions during the degradation of LLTO are sketched in Fig. 9a. In the colorized zone next to the cathode, slight Li excess

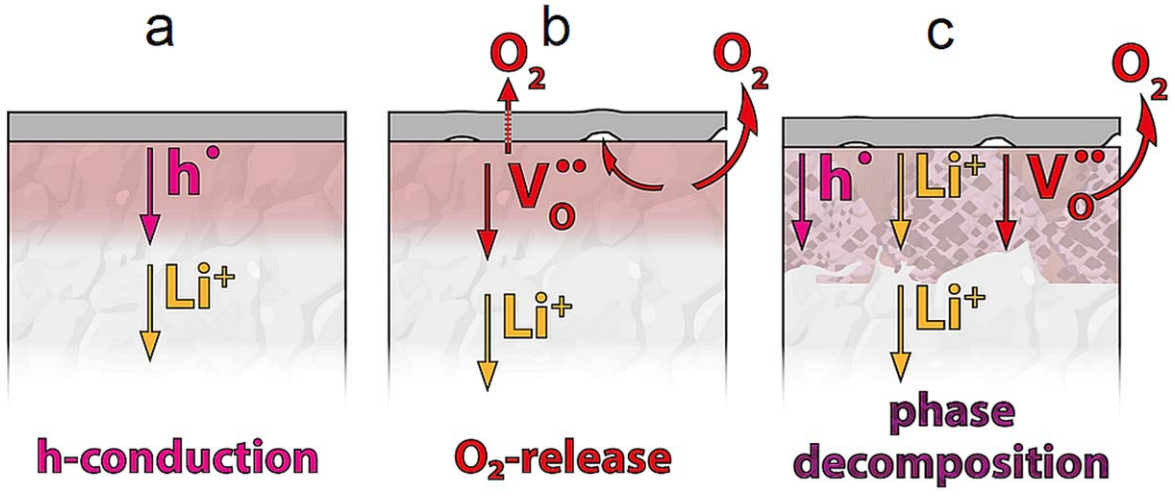

Figure 8. Schematics of the three suggested anode mechanisms: oxidation at the anode leads to either hole-conduction in LLTO (a), oxygen vacancy conduction (b) or decomposition into secondary phases (c) with Li, Oxygen and possibly hole conduction. O_2-release (i.e. oxygen oxidation) is the predominant redox reaction in mechanisms b and c.

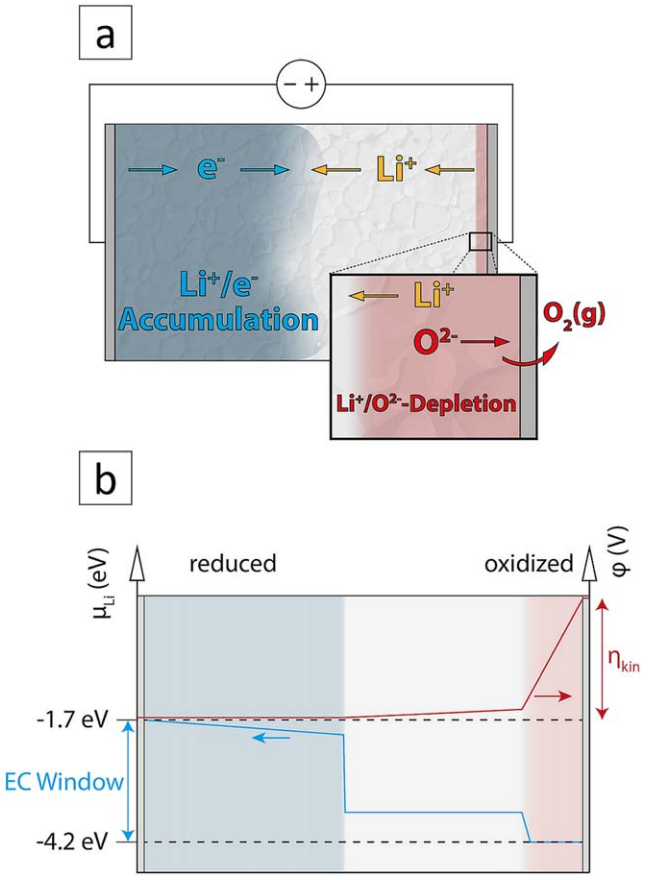

Figure 9. (a): Schematic of the proposed electrocoloration mechanism at the limit of about 2.5 V. (b): Schematic representation of Li chemical potential μ_{Li} (blue line, left y-axis), electrical potential ϕ (red line, right y-axis) and electrochemical (EC) stability window. Not drawn to scale.

stoichiometry is balanced by a small concentration of Ti^{3+}, which causes mixed ion and electron conductivity at a Li chemical potential around 1.7–1.8 V vs Li metal.[21] Recent own measurements showed that already at 2 V vs Li metal the electrolytic domain window is reached.[23] The width of the stability window was determined to be 2.5 V, according to OCV and coloration onset measurements. Hence, the high voltage stability limit lies at ca. 4.2–4.5 V vs Li metal and is therefore compatible with high-voltage cathodes. This stability limit is sufficient to use LLTO as a high voltage cathode coating materias.[26] Li^+ depletion at higher potentials is balanced by oxygen release at the anode. This reaction requires oxygen vacancy mobility, which is rate limiting during electrocoloration and limits the kinetics of the electrolyte decomposition. First principles DFT calculations predict an oxidative stability limit of 3.7 V.[18] However, this value is practically irrelevant, because it involves phase transitions that will not occur at room temperature.

Hence, we can suggest a qualitative picture of the overpotential distribution and Li activity distribution. Due to the high ionic conductivity and low current density within the uncolored and reduced zones, the electrical potential is almost constant there, as illustrated in Fig. 9b. Moreover, the total Li content varies only marginally within the reduced region and also the Li-ion chemical potential is virtually homogeneous. Nonetheless, the electron and lithium chemical potentials vary due to the different Ti^{3+} concentrations of colorized and uncolored zones. Most of the kinetic overpotential—the voltage above the stability limit—drops in the weakly conductive, heavily Li depleted zone next to the cathode.

Conclusions

Electrochemical and analytical experiments investigated the electrochemical stability window and the decomposition mechanisms of LLTO. Above 2.5 V between two ion-blocking electrodes, a coloration front starts moving from the reduction side (cathode) towards the anode. This coloration is caused by a slight overlithiation ($<10^{-4}$ p.f.u.), associated with Ti^{3+} formation at a potential of about 1.7–2 V vs lithium metal. The corresponding moderate electronic conductivity in the colored zone may limit the applicability of LLTO as an electrolyte but is not an irreversible decomposition reaction. On the other hand, next to the anode substantial Li depletion in a very confined zone of roughly one micrometer thickness occurs, as shown by LA-ICP-MS measurements. Li depletion starts at a potential of 4.2–4.5 V vs Li metal. We propose that oxygen evolution and oxygen vacancy formation, rather than charge balancing by electron holes, or formation of new, Li-free phases, occurs at the anode. The kinetics of this oxidation reaction is (at least partly) determined by the kinetics of combined oxide ion and Li-ion conduction and is thus rather sluggish. The slow anodic reaction also limits the velocity of the electrocoloration process. Our studies confirm that LLTO is suitable as an electrolyte or cathode protective layer towards typical high-voltage cathode materials, but becomes an electronic conductor in contact with virtually any anode material.

Acknowledgments

The authors gratefully acknowledge Austrian Science Fund (FWF) projects P 31437-N36 and P31165-N37 for financial support and *"Deutsches Elektronen-Synchrotron"* (DESY) for the allocation of beamtime.

ORCID

Andreas Limbeck https://orcid.org/0000-0001-5042-2445
Vedran Vonk https://orcid.org/0000-0001-9854-1101
Andreas Nenning https://orcid.org/0000-0001-9313-3731
Jürgen Fleig https://orcid.org/0000-0002-8401-6717

References

1. Y. Inaguma, C. Liquan, M. Itoh, T. Nakamura, T. Uchida, H. Ikuta, and M. Wakihara, *Solid State Commun.*, **86**, 689 (1993).
2. Y. J. Shan, L. Chen, Y. Inaguma, M. Itoh, and T. Nakamura, *J. Power Sources*, **54**, 397 (1995).
3. J. Emery, J. Y. Buzare, O. Bohnke, and J. L. Fourquet, *Solid State Ion.*, **99**, 41 (1997).
4. O. Bohnke, C. Bohnke, and J. L. Fourquet, *Solid State Ion.*, **91**, 21 (1996).
5. Y. Inaguma, Y. Matsui, Y.-J. Shan, M. Itoh, and T. Nakamura, *Solid State Ion.*, **79**, 91 (1995).
6. J.-S. Lee, K. S. Yoo, T. S. Kim, and H. J. Jung, *Solid State Ion.*, **98**, 15 (1997).
7. X. Cheng, J. Wang, W. Qiang, and B. Huang, *J. Am. Ceram. Soc.*, **103**, 3698 (2020).
8. Y. Harada, *Solid State Ion.*, **121**, 245 (1999).
9. M. Oguni, Y. Inaguma, M. Itoh, and T. Nakamura, *Solid State Commun.*, **91**, 627 (1994).
10. Y. Hirakoso, Y. Harada, J. Kuwano, Y. Saito, Y. Ishikawa, and T. Eguchi, *Key Eng. Mater.*, **169–170**, 209 (1999).
11. X. Gao, C. A. J. Fisher, T. Kimura, Y. H. Ikuhara, H. Moriwake, A. Kuwabara, H. Oki, T. Tojigamori, R. Huang, and Y. Ikuhara, *Chem. Mater.*, **25**, 1607 (2013).
12. Y. Harada, T. Ishigaki, H. Kawai, and J. Kuwano, *Solid State Ion.*, **108**, 407 (1998).
13. J. Wu, L. Chen, T. Song, Z. Zou, J. Gao, W. Zhang, and S. Shi, *Funct. Mater. Lett.*, **10**, 1730002 (2017).
14. X. Guo, P. S. Maram, and A. Navrotsky, *J. Mater. Chem. A*, **5**, 12951 (2017).
15. Z. Li, C. Li, X. Liu, L. Cao, P. Li, R. Wei, X. Li, D. Guo, K.-W. Huang, and Z. Lai, *Energy Environ. Sci.*, **14**, 3152 (2021).
16. Y. Inaguma and M. Nakashima, *J. Power Sources*, **228**, 250 (2013).
17. R. E. Warburton et al., *Chem. Mater.*, **33**, 8447 (2021).
18. Y. Zhu, X. He, and Y. Mo, *ACS Appl. Mater. Interfaces*, **7**, 23685 (2015).
19. M. Bertrand, S. Rousselot, D. Aymé-Perrot, and M. Dollé, *Mater. Adv.*, **2**, 2989 (2021).
20. T. Binninger, A. Marcolongo, M. Mottet, V. Weber, and T. Laino, *J. Mater. Chem. A*, **8**, 1347 (2020).
21. P. Birke, S. Scharner, R. A. Huggins, and W. Weppner, *J. Electrochem. Soc.*, **144**, L167 (1997).
22. C. Hua, X. Fang, Z. Wang, and L. Chen, *Electrochem. Commun.*, **32**, 5 (2013).
23. J. Ring, J. Nenning, and J. Fleig, *Journal of The Electrochemical Society*, **170**, 050530 (2023).
24. L. Zhang et al., *Nat. Commun.*, **11**, 3490 (2020).
25. S. Wenzel, T. Leichtweiss, D. Krüger, J. Sann, and J. Janek, *Solid State Ion.*, **278**, 98 (2015).

26. D. Qian, B. Xu, H.-M. Cho, T. Hatsukade, K. J. Carroll, and Y. S. Meng, *Chem. Mater.*, **24**, 2744 (2012).
27. Y. Wu, H. Cui, X. Liu, X. Zhong, Z. Li, C. Wang, and S. Dmytro, *J. Solid State Electrochem.*, **27**, 1501 (2023).
28. S. Ohta, T. Kobayashi, and T. Asaoka, *J. Power Sources*, **196**, 3342 (2011).
29. F. Han, Y. Zhu, X. He, Y. Mo, and C. Wang, *Adv. Energy Mater.*, **6**, 1501590 (2016).
30. S. Smetaczek et al., *J. Mater. Chem. A*, **9**, 15226 (2021).
31. O. H. Seeck et al., *J. Synchrotron Radiat.*, **19**, 30 (2012).
32. J. Blanc and D. L. Staebler, *Phys. Rev. B*, **4**, 3548 (1971).
33. M. J. Wang, J. B. Wolfenstine, and J. Sakamoto, *Adv. Funct. Mater.*, **30**, 1909140 (2020).
34. O. Bohnke, S. Lorant, M. Roffat, and P. Berger, *Solid State Ion.*, **262**, 563 (2014).
35. G. Larraz, A. Orera, and M. L. Sanjuán, *J. Mater. Chem. A*, **1**, 11419 (2013).
36. T. Zinkevich, B. Schwarz, P. Braun, A. Weber, H. Ehrenberg, and S. Indris, *Solid State Ion.*, **357**, 115486 (2020).
37. R. Waser, T. Baiatu, and K.-H. Härdtl, *J. Am. Ceram. Soc.*, **73**, 1654 (1990).
38. C. Rodenbücher, K. Szot, D. Wrana, B. R. Jany, F. Krok, and C. Korte, *J. Phys.: Energy*, **2**, 034008 (2020).
39. I. Yokota, *J. Phys. Soc. Jpn.*, **16**, 2213 (1961).
40. S. Miyatani, *J. Phys. Soc. Jpn.*, **50**, 1595 (1981).
41. M. H. Hebb, *J. Chem. Phys.*, **20**, 185 (1952).
42. C. Wagner and Z. Für Elektrochem, *Berichte Bunsenges. Für Phys. Chem.*, **60**, 4 (1956).
43. T. Shimonosono, Y. Hirata, Y. Ehira, S. Sameshima, T. Horita, and H. Yokokawa, *Solid State Ion.*, **174**, 27 (2004).
44. D. Geng, N. Ding, T. S. A. Hor, S. W. Chien, Z. Liu, D. Wuu, X. Sun, and Y. Zong, *Adv. Energy Mater.*, **6**, 1502164 (2016).
45. M. Siebenhofer et al., *J. Eur. Ceram. Soc.*, **42**, 1510 (2022).
46. M. Kubicek, A. Wachter-Welzl, D. Rettenwander, R. Wagner, S. Berendts, R. Uecker, G. Amthauer, H. Hutter, and J. Fleig, *Chem. Mater.*, **29**, 7189 (2017).
47. F. Aguesse, V. Roddatis, J. Roqueta, P. García, D. Pergolesi, J. Santiso, and J. A. Kilner, *Solid State Ion.*, **272**, 1 (2015).